

Capillary force-driven particle orientation in rod networks

Lingyue Liu*,¹ Sebastian Gassenmeier,¹ and Erin Koos*¹

¹*KU Leuven, Department of Chemical Engineering,
Soft Matter, Rheology and Technology, 3001 Leuven, Belgium.*

arXiv:2503.18744v1 [cond-mat.soft] 24 Mar 2025

*[htbp]

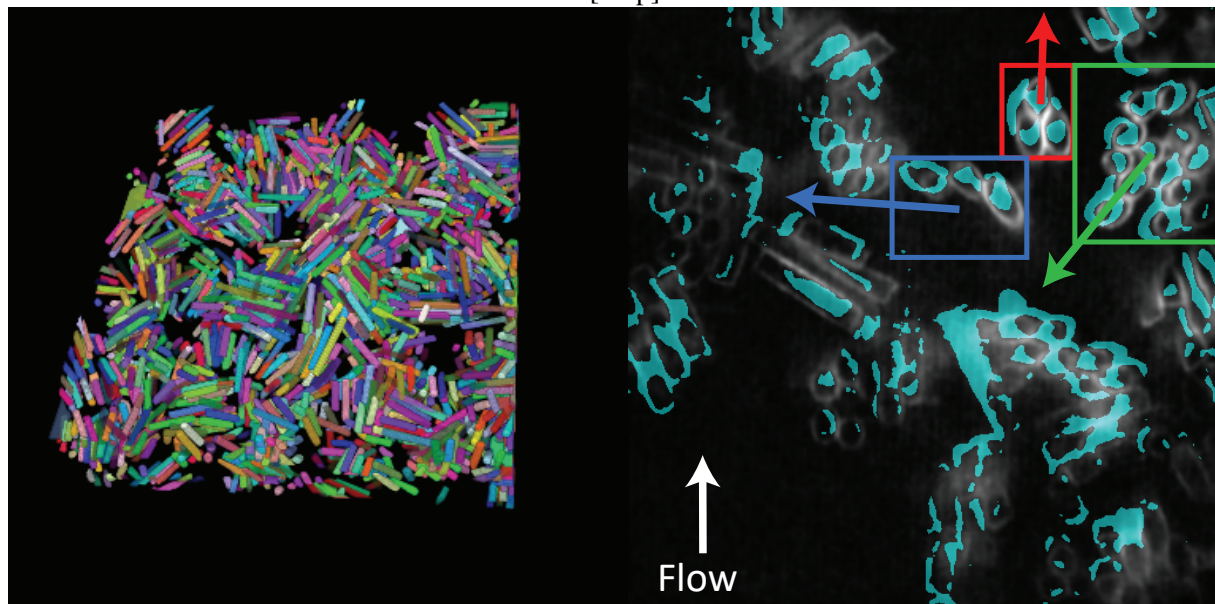


FIG. 1. Graphical Abstract.

ABSTRACT

Capillary suspensions containing anisotropic rod particles exhibit complex microstructural behaviors. Our study investigates the orientation, network formation, and rheological properties of glass microrods in capillary suspensions with varying secondary liquid volumes. Using confocal microscopy, rheometry, and rheoconfocal techniques, we reveal how capillary forces affect particle alignment and movement, and consequently, the microstructure of the samples. As the volume fraction of the secondary liquid increases, the structure of the rod network exhibits a transition from point-to-point contact to side-to-side aligned clusters. This structural change leads to pronounced changes in coordination number, clustering coefficient, and particle orientation distribution. In contrast to spherical systems, the average clustering coefficient decreases with increasing coordination number, denoting the formation of particle clusters with complex configurations instead of solely side-to-side alignment. Rheological measurements demonstrate the sensitivity of rod-based networks to deformation, with shorter linear viscoelastic regions compared to spherical particle systems. The research provides insights into designing advanced materials with tunable mechanical properties through controlled particle interactions.

HIGHLIGHTS

1. Rod-based capillary suspensions are sensitive to secondary liquid volume fractions as increased secondary liquid transforms rod particle contact type from point-to-point to side-to-side contacts. The average side-to-side contact probability is positively correlated to the clustering coefficient and negatively correlated to the coordination number.
2. Unlike spherical systems, the average clustering coefficient decreases with increasing coordination number, indicating the formation of complex particle cluster configurations beyond simple side-to-side alignment.
3. Rod-based capillary suspensions exhibit higher sensitivity to deformation and samples with higher side-to-side contact probability demonstrate increased viscoplastic fragility.
4. During yielding, particle clusters move in completely different directions with collective rotation, while maintaining their internal structure.

KEYWORDS

Capillary suspension; Anisotropic particle; Rheology; Yielding; Network structure

* Corresponding author: lingyue.liu@kuleuven.be erin.koos@kuleuven.be

I. INTRODUCTION

Anisotropic particles, such as plates [1], fibers [2], and rods [3, 4], exhibit distinct properties, including orientation-dependent interactions, enhanced percolation, and directional assembly. Moreover, these particles can introduce unique functionalities, such as electrical or thermal conductivity, optical anisotropy, and mechanical reinforcement, which are highly desirable in various industrial applications [5]. Common spherical models fail to describe rod particle suspensions because their elongated geometry creates orientation-dependent hydrodynamic forces and rotational dynamics. Different from spherical particles that rotate freely, anisotropic particles tumble and exhibit transient properties depending on their orientation [6]. In semi-dilute suspensions, particle-particle contact interactions contribute to the viscosity with a quadratic dependency to particle volume fraction [2]. As the volume fraction keeps increasing, the minimum separation between the nearest neighboring particles decreases, and a yield stress is developed when they are in repulsion, forming a jammed network. The network is capable of elastically accommodating stress until the yield stress is reached and subsequent breakdown and shear-thinning behavior is observed [7]. Using particles with higher aspect ratios, the maximum packing and the percolation threshold is reduced, allowing percolating networks to form at lower particle density [6, 7].

Capillary suspensions, a class of materials formed by adding a small amount of immiscible secondary fluid to a normal suspension, have attracted attention in recent years due to their unique rheological properties. From an industrial perspective, capillary suspensions offer a promising route to formulate art works [8], porous ceramics [9] or precursors for 3D printing [10, 11]. The added secondary fluid forms a sample-spanning network of bridged particles, which drastically changes the mechanical properties by introducing a yield stress at a much lower particle volume fraction in comparison to the network percolating threshold [12]. While the majority of the studies on capillary suspensions have been focusing on spherical particles [13–16], there are certain ones with anisotropic (non-arbitrarily-shaped) microparticles, with oblate [17, 18] and prolate particles [18, 19]. The incorporation of anisotropic particles can extend the range of achievable properties and enable the development of novel, high-performance materials.

The local microstructure of capillary suspensions which governs the system can be tuned by changing the several key factors, particularly particle shape [18], aspect ratio [6], and secondary fluid volume fraction [20]. At small fractions of secondary liquid, increasing the liquid volume fraction leads to a higher probability of bridge formation between adjacent particles with larger

volume fractions resulting in more robust and stable bridges. As the amount of secondary liquid increases, both coordination number and clustering coefficient increase positively, reflecting the structural transitions from pendular to funicular and further to capillary states [20, 21]. This effect is particularly pronounced in anisotropic particle network, where the interplay between aspect ratio and secondary fluid creates complex network structures [18]. Within the networks, the precise orientation of individual particle, the local cluster configuration, and the internal structures' response to external deformation remains unknown.

In this context, the present paper aims to address fundamental questions about capillary suspensions containing rod-like particles investigating the influence of the capillary interaction on particle orientation, network formation and structural stability. The response of these systems to external stresses is explored using a combining rheometer and confocal microscope. Here, we aim to establish a comprehensive understanding of these complex systems and develop principles for designing and optimizing capillary suspensions for targeted performance.

II. MATERIALS AND METHODS

A. Sample preparation

Glass microrods (PF-60S, Nippon Electric Glass Co., Ltd.) with an average diameter of $6 \pm 0.01 \mu\text{m}$ and an aspect ratio of 4 ± 1 were used as the main structure of the capillary suspensions. The microrods, with a density of 2.6 g/cm^3 and a refractive index of 1.56, were fluorescently dyed with rhodamine B isothiocyanate (RBITC, Sigma-Aldrich). The bulk phase of the capillary suspensions consisted of a mixture of 82.2 wt% cinnamon bark oil ($> 99 \%$, Sigma-Aldrich) and 17.8 wt% 1,2-cyclohexane dicarboxylic acid diisononyl ester (Hexamoll DINCH, BASF). The oil mixture had a refractive index of $n = 1.56$, matching that of the microrods. The density of this mixture is 1.01 g/ml. The secondary liquid was a mixture of 50 vol% glycerol ($> 99.5 \%$, Carl Roth) and 50 vol% ultrapure water (Arium 611DI, Sartorius Stedim Biotech) with a $n = 1.4$ and a density of 1.12 g/ml. While this solution did not match the refractive index of the particles and bulk liquid, the percentage of the glycerol is kept low to prevent an elevated viscosity, which would require excessive energy input during dispersion. High energy input during dispersion of the rods and breakup of the secondary liquid droplets accelerated cinnamon oil oxidation, which modified the bulk liquid refractive index, minimizing the visual depth.

15 vol% rods were dispersed in the bulk liquid to ensure homogeneous wetting and prevent aggregation. The corresponding volumes of secondary liquid (0-0.75 vol%) were then dispersed using an ultrasonic horn of 3.175 mm diameter (Digital Sonifier model 450, Branson Ultrasonics corporation) at a 10 % amplitude for 2 s. The interfacial tension between the secondary liquid and the bulk liquid mixture is 11.7 ± 0.2 mN/m, as measured with a drop tensiometer (Attension, Biolin Scientific) at a room temperature (20.5 ± 1 °C) using a frame rate of 20 FPS and a duration of 30 min. The value did not fluctuate throughout the experiment period. The three-phase contact angle θ of the rods was determined using confocal images of the particles at the liquid-liquid interface in a microchannel, following the method of Allard et al. [13]. The microrods had a low contact angle approaching 0° (Supplementary Fig. S1).

B. Rheological measurements

A stress-controlled rheometer MCR702 (Anton Paar) with an 8 mm top plate and a 50 mm bottom plate geometry was used to perform oscillatory measurements. A double motor setup was used for enhanced sensitivity. All amplitude sweeps were conducted at an angular frequency of 10 rad/s. Frequency sweeps with a shear strain of 0.005 % ensured the frequency independence of the gel structures between 0.1 rad/s and 10 rad/s. The oscillatory stress sweeps were performed with a maximum stress of 20 Pa below the yield stress.

The sample was loaded onto the rheometer with a spatula. The top plate was lowered to a gap of 3 mm, after which the compression was recorded. The top plate was then lowered to the trim position of 1.025 mm, 25 μm above the measuring position, with a uniaxial velocity of 19.75 $\mu\text{m/s}$. This allowed the extra sample at the edges to be scraped off prior to other measurements. Afterwards, the top plate was lowered to the measurement gap of 1 mm. The normal force, i.e., the thrust on the plate, was recorded during both the gap lowering and oscillating experiments.

C. Confocal and rheoconfocal microscopy

Samples were spread onto a 22 \times 40 mm cover glass (Menzel-Gläser) using a spatula. The samples were then transferred to a Leica TCS SP8 inverted confocal laser scanning microscope (Leica Microsystems GmbH, Wetzlar, Germany). Imaging of the particle structures was performed using a glycerol immersion objective with 63 \times magnification and a numerical aperture of 1.3.

Solid-state lasers with wavelengths of 488 nm and 552 nm were used to excite PromoFluor-488 (liquid channel) and rhodamine B isothiocyanate (particle channel), respectively. To reconstruct the 3D structure of the capillary suspension, 3D image stacks were taken, each consisting of x - y planes of size $246 \times 246 \mu\text{m}$ and a resolution of 1024×1024 pixels. The z resolution was set to 3 micrographs per $1 \mu\text{m}$, the intensity loss over z due to the high refractive index of the system allowed 210 micrographs, with an equivalent of $70 \mu\text{m}$, to be taken before micrographs become inaccessible for further analysis.

To observe sample deformation under shear, a stress-controlled rheometer (MCR302 WSP, Anton Paar) was mounted on a microscope stand (IX71, Olympus) equipped with a fast-scanning confocal microscope (VT HAWK, Visitech) to perform simultaneous imaging and rheological measurements. A stiff sapphire glass window with a diameter of 30 mm and a thickness of $170 \mu\text{m}$ was glued into a custom-made holder as the bottom geometry. A Hamamatsu EMCCD camera recorded image sequences with exposure times of 50 ms in 2D and 100 ms in 3D. Imaging was done using two oil objectives (UPlanSApo, Olympus) with magnifications of $20\times$ and $60\times$ and numerical apertures of 0.85 and 1.35, resulting in pixel sizes of $0.80 \mu\text{m}$ and $0.27 \mu\text{m}$, respectively. The objectives were mounted on a piezo actuator to perform 3D scans in the z -direction. The rheometer was positioned on an xy -gantry system (Screw Drive LRT Gantry, Zaber) to reposition it relative to the microscope, allowing measurement at different radial positions along the parallel plate geometry, which was a 15 mm stainless steel plate. The imaging plane was positioned 1 mm from the edge of the plate. The rheometer applied the input strain at $2/3$ of the plate radius, with calculation mode DIN 53018 R2/3, allowing local strain to be calculated by $\gamma_{est,0} \cdot \frac{3}{2} \cdot \frac{6.5 \text{ mm}}{7.5 \text{ mm}}$. Rheological measurements were performed at angular frequency of 10 rad/s with gaps between $200 \mu\text{m}$ and $300 \mu\text{m}$, minimizing the effect of potential confinement. A doctor blade was used to load thin capillary suspension layers, avoiding solid phase compaction due to such small gaps.

D. Image processing and particle tracking

The confocal micrographs of the static structure were exported as two separate channels for fluorescence response of the two lasers illuminating the microrods and secondary liquid. The microparticle channel (Fig. 2a) was denoised in Fiji using subtract background function with a rolling ball radius of 50 pixels. Next, we auto local thresholded each micrograph using the Niblack method with a 15-pixel radius to sharpen and identify edges. This process allowed for the separate

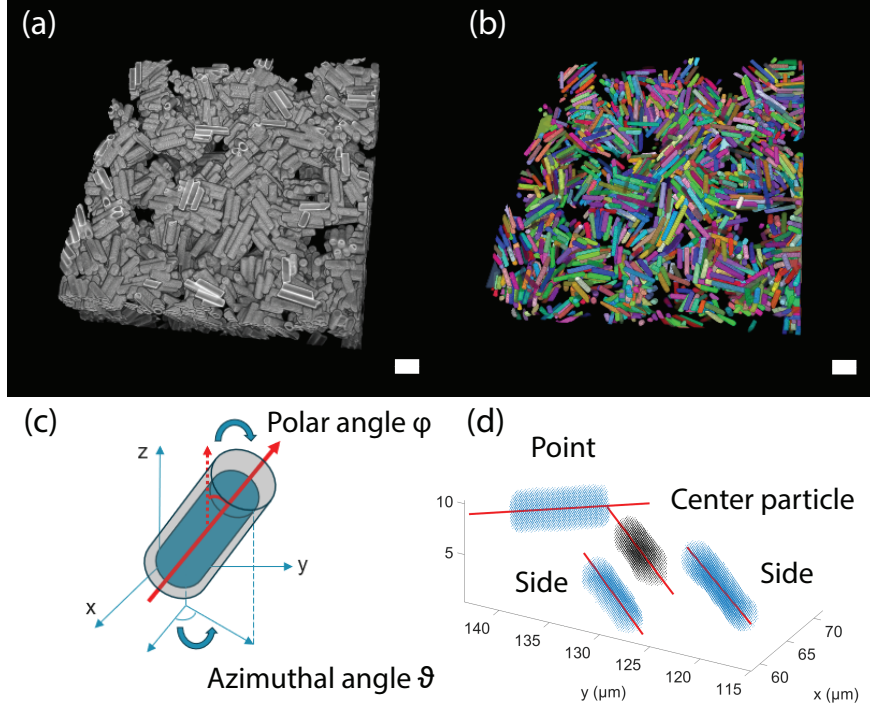


FIG. 2. (a) 3D scanned micrographs of a capillary suspension gel with 15 vol% of 6 μm rods with 0.5625 % secondary liquid (b) detected and reconstructed 3D view of the sample with each particle colored differently, the scale bars are 20 μm . (c) Rod orientation resolved by azimuthal angle ϑ and polar angle ϕ (d) An example of the determination of particle contact types, where the black voxels are the center particle and blue voxels are neighboring particles. The red lines represent the calculated major axes. The particles appear to be not in direct contact with each other due to the exclusion of their fluorescent outlines.

detection of enclosed areas based on their fluorescent boundaries. We then tracked and linked these enclosed areas (Fig. 2b) using centroid distance criteria through a modified MATLAB 3D tracking code, adapted from the algorithm developed by E.R. Weeks and J.C. Crocker [22]. The detected image appears sparser in comparison to the original image due to the fact that the shells are discarded and the particles are reconstructed using the enclosed center areas within the fluorescent outlines. These outer shell signals have an approximate length of 0.6 μm , resulting in a lower apparent solid volume fraction.

We resolve the orientation of the individual rods, constituted by their respective voxel lists, by solving the eigenvalue problem of the moment of inertia matrix $I_{ij} = m_{\alpha} r_{\alpha}^2 \delta_{ij} - m_{\alpha} r_{\alpha i} r_{\alpha j}$ for each rod, which is symmetric and therefore yields positive eigenvalues and an orthonormal eigenbasis. We are then able to discriminate the moment of inertia in the longitudinal direction of the rod

and set the corresponding eigenvector as the rod orientation. This orientation is transformed to spherical coordinates, yielding a polar angle θ ($0 \leq \theta \leq \frac{\pi}{2}$) as the angle formed by the positive z-axis (polar axis) and the radial line and the azimuthal angle ϑ ($0 \leq \vartheta \leq \pi$) which is the angle of rotation around the z-axis (Fig. 2c).

To quantify the network structure, two general parameters are introduced: the coordination number (z) and the clustering coefficient (c). The coordination number is the number of neighboring particles that are in contact with each particle. Based on the averaged outline thickness of the detected fluorescent shell, a 3 μm proximity criterion was established for contact determination, accounting for the spatial resolution limitations of the confocal microscopy system. Unlike spherical system with a maximal coordination number of 12 [20], this maximal value is related to the average aspect ratio of the applied rods. The clustering coefficient is an indication of the degree of aggregation, defined as $c = \frac{2e}{z(z-1)}$, where e is the number of connections between the neighboring particles [20]. The clustering coefficient c therefore divides the neighbor-connectivity by the maximum possible connectivity and yields values from 0 to 1 for all systems, denoting a well-distributed or a fully clustered network, respectively.

To further quantify the morphology of the system, the particle contacts can be categorized into two types, point-to-point or side-to-side, as shown in Fig. 2d). Due to the unevenness of the rod particle ends, end-to-end contacts are not statistically significant in this study. As a general parameter, we introduce the side contact ratio since side-to-side contact pairs exhibit a much stronger capillary force due to the elevated contact area in comparison to the point-to-point contact pairs. The enhanced capillary forces promote aggregation, resulting in a rod cluster self-aligning in the same direction. Therefore, the criteria for side-to-side contact is that whether the touching particles are aligning in the same direction ($\pm 10^\circ$ for both θ and ϑ , Fig. 2d).

III. RESULTS AND DISCUSSION

A. Microstructure

Example micrographs of the network captured via a confocal microscopy are shown in Fig. 3. The micrographs, showing slices near the bottom plate, reveal a pronounced evolution in microstructure with increasing secondary fluid content. In Fig. 3a, the suspension system shows a relatively uniform, compact distribution of rod particles that sediment due to their weight and lack

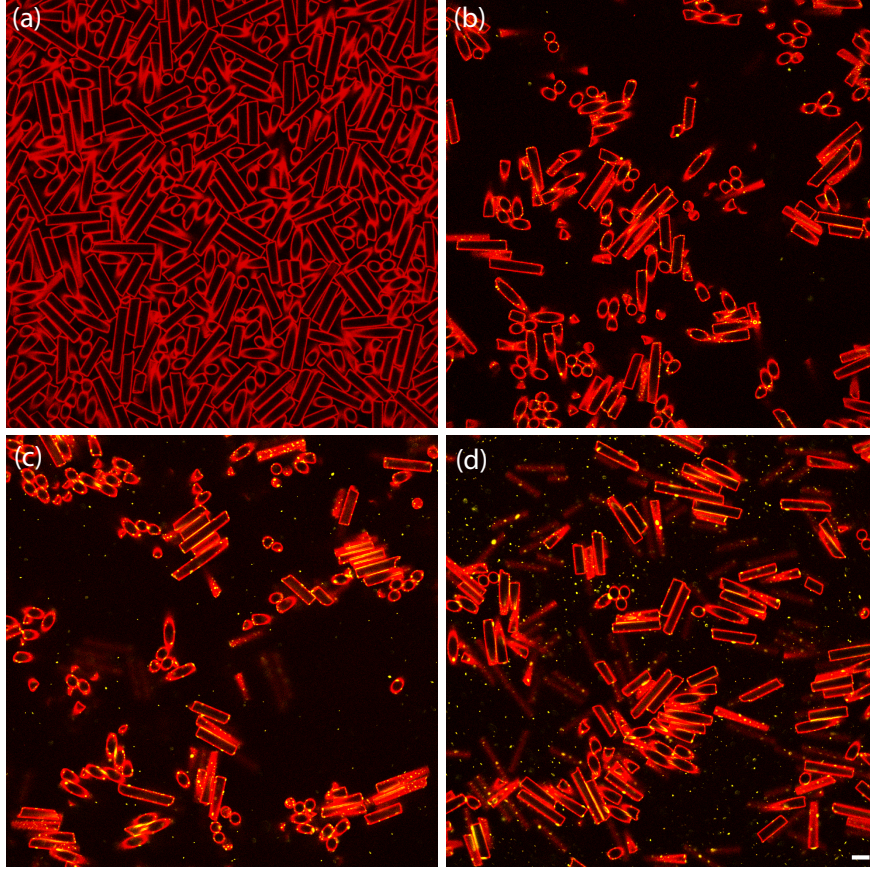


FIG. 3. Confocal micrographs of capillary suspension with different amount of secondary liquid (a) 0 % ($\phi_{\text{sec}}/\phi_{\text{solid}} = 0.0$ %) (b) 0.375 % ($\phi_{\text{sec}}/\phi_{\text{solid}} = 2.5$ %) (c) 0.5625 % ($\phi_{\text{sec}}/\phi_{\text{solid}} = 3.75$ %) (d) 0.75 % ($\phi_{\text{sec}}/\phi_{\text{solid}} = 5$ %), the scale bar is 10 μm .

of interparticle forces. The majority of the rods lay flat (parallel to the image plane and perpendicular to gravity) with a polar angle approaching to 90° . The maximum packing $\phi_{m,rod}$ of rods with an aspect ratio AR is given by Eq. 1 [6],

$$\phi_{m,rod} = \frac{2}{0.321AR + 3.02} \quad (1)$$

For rod-shaped particles of $AR = 4 \pm 1$, the maximum packing decreases slightly from $\phi_{m,rod} = 64$ % for spheres to $\phi_{m,sph} = 46.5$ vol% [23]. The effective volume fraction calculated in the sedimented rods in Fig. 3a is 44.1 %, close to the theoretical value. However, due to the rod length distribution, the real maximum packing should be higher than the theoretical value [24]. A marked difference is observed with the addition of secondary fluid, as shown in Fig. 3b-c where a gel-forming structure is observed with capillary bridges shown in yellow. The gel network, formed with 15 vol% rods, is much lower than the estimation of the percolation threshold of

$0.8\phi_{m,rod} = 37.2 \text{ vol\%}$. Therefore, the capillary force stemming from surface tension and capillary pressure give rises to gel structure in these capillary suspension samples [25–27].

As the secondary fluid content increases, the particle aggregates progressively, characterized by clusters of rods with preferential side-to-side alignment, as shown in Supplementary Fig. S2. This clustering behavior is attributed to the capillary force increase by introducing excessive secondary fluid yielding a transition from point-to-point to side-to-side contacts. The point contact capillary force is estimated using the model developed by Rabinovich et al., as shown in Eq. 2 [28],

$$F_{cap,point} = \frac{2\pi r \gamma \cos \theta}{1 + \frac{S}{2C}} \quad (2)$$

$$\text{for } C = \frac{S}{2} \left(-1 + \sqrt{1 + \frac{2V}{\pi r S^2}} \right)$$

where γ is the interfacial tension, the three-phase contact angle is θ , r is the radius of the rod, V is the individual bridge volume and S is the separation distance. Using a cylindrical approximation to find the bridge volume, the corresponding capillary force is approximately 200 nN.

In wet spherical granular systems, bridges are generally toroidal, with the possibility of forming trimer, pentamer, or filled tetrahedra [29]. In rod systems, however, the formation of larger bridges are observed less frequently when the secondary liquid preferably wets the solid particles [26]. This is because the filled bridges are not thermodynamically stable and tend to separate when particles are in close contact in a side-to-side structure [26]. Based on the critical separation model proposed for three-cylinder system [27], as long as the separation distance $S_{crit}/r < 0.28$, the capillary bridges remain separate for $\theta = 30^\circ$ rods, as shown in Supplementary Fig. S3b. Above this distance, the thermally equilibrated stable bridges with high menisci merge again and fill the internal gap [25–27]. The critical separation distance in the system applied in this study is $0.8 \mu\text{m}$, exceeding the maximum bridge height, the separation of the bridge is confirmed through the observation of the micrograph.

Therefore, toroidal bridges between two rods stretch and expand over the whole length of the rods, and the capillary force per unit length $F_{cap,side}/L$ is given in Eq. 3 [27],

$$F_{cap,side}/L = 2\gamma \sin(\alpha + \theta) + 2\gamma \sin \alpha (r/R) \quad (3)$$

where the angle between the line connecting the centers of the cylinders and the radius to the liquid-liquid boundary is α , and R is the curvature of the liquid surface, as shown in the schematic shown in Fig. S3a. By manually categorizing over 20 samples for each contact type (point-to-point contacts and side-to-side contact) in the 3D stacks of Fig. 3d (Supplementary Fig. S4), the

observed average bridge height is approximately $0.6 \pm 0.1 \mu\text{m}$, and the averaged width of the bridges is to $2.4 \pm 0.1 \mu\text{m}$, despite their high variability in bridge length. Taking these values into the account the calculated angle $\alpha = 25^\circ$, the contact angle θ is 28° , which shows their strong hydrophilic nature but slightly higher than the value measured using the microchannel liquid-liquid interface contact angle technique (0°) shown in supplementary Fig. S1. By applying the θ and α into Eq. 3, $r/R \approx 5.97$ and the resulting capillary force per unit length is 0.078 N/m . Taking the average rod length (L) into consideration, the total capillary force is roughly $1.87 \mu\text{N}$. Given these values, the ratio between $F_{cap,side}$ and $F_{cap,point}$ is up to 935 %, which promotes side-to-side particle attraction. Regarding the role of particle weight, if we consider a cluster of rods suspended from a single bridge, gravity only overcomes the capillary force for $1.9 \cdot 10^5$ rods (side-to-side) or $2 \cdot 10^4$ (point-to-point). These values indicate that gravitation can be ignored as the particle number in the field of view is in the range of 10^3 . To better assess the influence of secondary liquid, we can calculate the particle orientation.

1. Polar angle and azimuthal angle

With increasing secondary liquid fractions, the alignment of the particles with the glass plate (parallel to the image plane in Fig. 3) decreases. This phenomenon is particularly clear for 0.375 vol% secondary liquid, shown in Fig. 3b, where the majority of particles do not align parallel to the glass plate. The polar angle probability distribution is as shown in Fig. 4a, where the theoretical probability of finding a randomly distributed particle with polar angle φ within the range $[\varphi_{start}, \varphi_{end}]$ is shown using the black curve. This probability can be expressed as,

$$\mathbb{P}(\varphi_{start \rightarrow end}) = \frac{A(\varphi_{start \rightarrow end})}{A_{0 \rightarrow \frac{\pi}{2}}} = \frac{\int_0^{2\pi} \int_{\varphi_{start}}^{\varphi_{end}} L^2 \sin \varphi d\varphi d\vartheta}{2\pi L^2} \quad (4)$$

where the the particle length L is radial distance in the spherical coordinate system. Without secondary liquid, the polar angle (φ) distribution remains below the theoretical curve for $\phi < 70^\circ$, indicating the majority of the rods lying against the substrate due to gravity. The capillary force between particles begins to become effective as secondary liquid bridges are formed, as shown by the decrease in possibility in higher polar angles and increase in the probability at lower angles. As the liquid volume increases, the probability distribution of the polar angles at lower angles increases, approaching the theoretical value. This behavior can be attributed to the elevated point-to-point interparticle contacts. However, as the liquid volume approaches 0.75 %, the probability

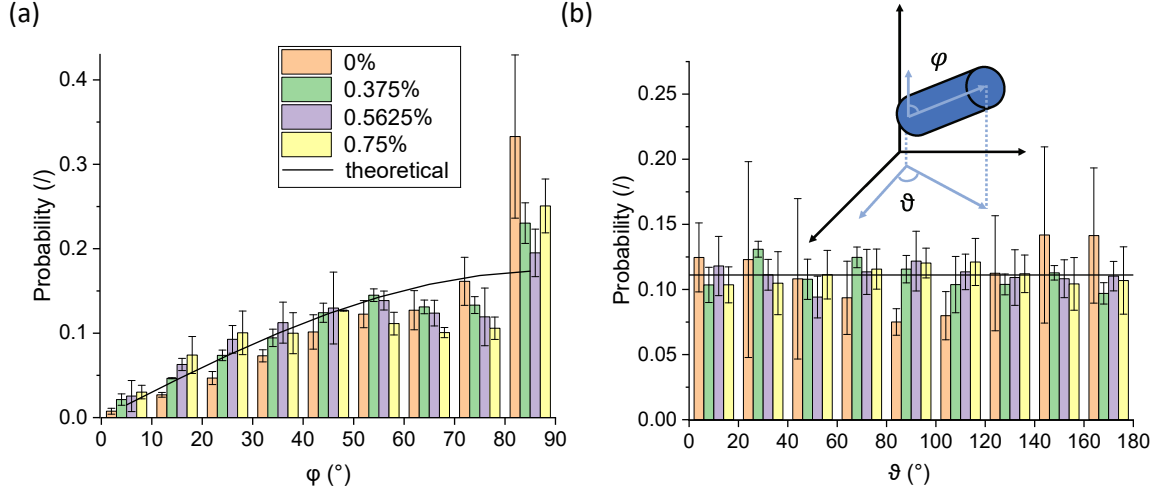


FIG. 4. Probability distribution of (a) polar angles (ϕ), ranging from 0° (perpendicular to the substrate) to 90° (parallel to the substrate) and (b) azimuthal angles (ϑ), ranging from 0° to 180° . With a simplified sketch of rod orientation attached.

of finding particles located at polar angles $80^\circ < \phi < 90^\circ$ increases. This occurs because the elevated liquid level enables much more probable side-to-side contact between particles, especially when particles face a flat substrate (bottom plate) rather than highly curved interparticle surfaces. When in contact with both configurations, the orientation competition lies between side-to-side (particle/cluster-glass) and point-to-point (particle/cluster-particle) capillary bridges. The side-to-side contacts with high capillary forces may result in preferential high polar angles, as can be seen in Fig. S5d. This biased structure approaching the bottom slide is not reported in spherical systems where only point-to point contact exist [13, 30].

The azimuthal angle (Fig. 4b) does not seem to be affected by the increasing amount of secondary liquids, following the theoretical line for a random orientation. The only exception to this homogeneous distribution is the 0 vol% sample where the capillary force is absent. The suspension system exhibits larger error bars and decrease in the probability of finding rods with $80^\circ < \theta < 120^\circ$, indicating substantial unity in particle orientations. Such a bias in the azimuthal angle may be due to the influence of sample loading (e.g. strain caused by the spatula or tilting of the slide).

2. Coordination number and clustering coefficient

Since there are clearly differences in the microstructure resulting in the apparent bias in polar angle, we also quantified the coordination number and clustering coefficients [20], as shown in Fig. 5a and 5b respectively. In Fig. 5a, the coordination number distribution shows the suspension system without secondary fluid ($\phi_{sec} = 0\%$) has a broad distribution of coordination numbers ($z = 8-12$) with mean coordination number of 8.9 and standard deviation 1.0. These values are consistent with a compact contact networks, mirroring that typically found in granular media ($z = 9-10$) [31]. In contrast, the systems with added secondary fluid predominantly exhibit lower coordination numbers ($z = 2-5$), with a mean coordination number of $z = 4.2$ and a standard deviation of 0.1. The decreased number in individual neighboring particles denotes a higher effective volume, resulting in a space-spanning network [20]. Despite the apparent differences in structure shown in Fig. 3 with $\phi_{sec} = 0.375\%$ having smaller clusters and $\phi_{sec} = 0.75\%$ having larger, no significant difference between the coordination number distributions is visible.

The analysis of particle contact topology reveals distinct trends in the microstructural organization of rod-based capillary suspension. Along with the averaged clustering coefficient, they are plotted over the coordination number, as shown in Fig. 5c and 5e. Particles with coordination numbers $z < 2$ for suspension systems and $z < 1$ for capillary suspension systems are primarily located at the edges of image stacks and are therefore excluded. Meanwhile, the particles with coordination numbers $z > 12$ for suspension systems and $z > 10$ for capillary suspension systems are not statistically significant given their small number. Therefore, both cases are eliminated from the figures. The side-to-side contact probability exhibits a monotonic decrease with increasing coordination number, with maximal values observed at low coordination numbers ($z = 2-4$). The introduction of secondary fluid significantly enhances the probability of side-to-side contacts compared to the suspension system as capillary forces become significant (Eq. 3), with this effect strengthening local clusters as secondary liquid volume increases.

The clustering coefficient distribution in Fig. 5b demonstrates a particularly special behavior where the suspension system ($\phi_{sec} = 0\%$) shows a pronounced peak at higher clustering coefficients ($c \approx 0.3$) and a quasi-normal distribution (except for $c < 0.2$). Meanwhile, systems with secondary fluid display more uniform distributions across middle clustering coefficient values ($c = 0.2-0.7$). This suggests that while secondary fluid promotes stable contacts between particles, it leads to more diverse local structural arrangements (see Fig. 5d for examples) rather than

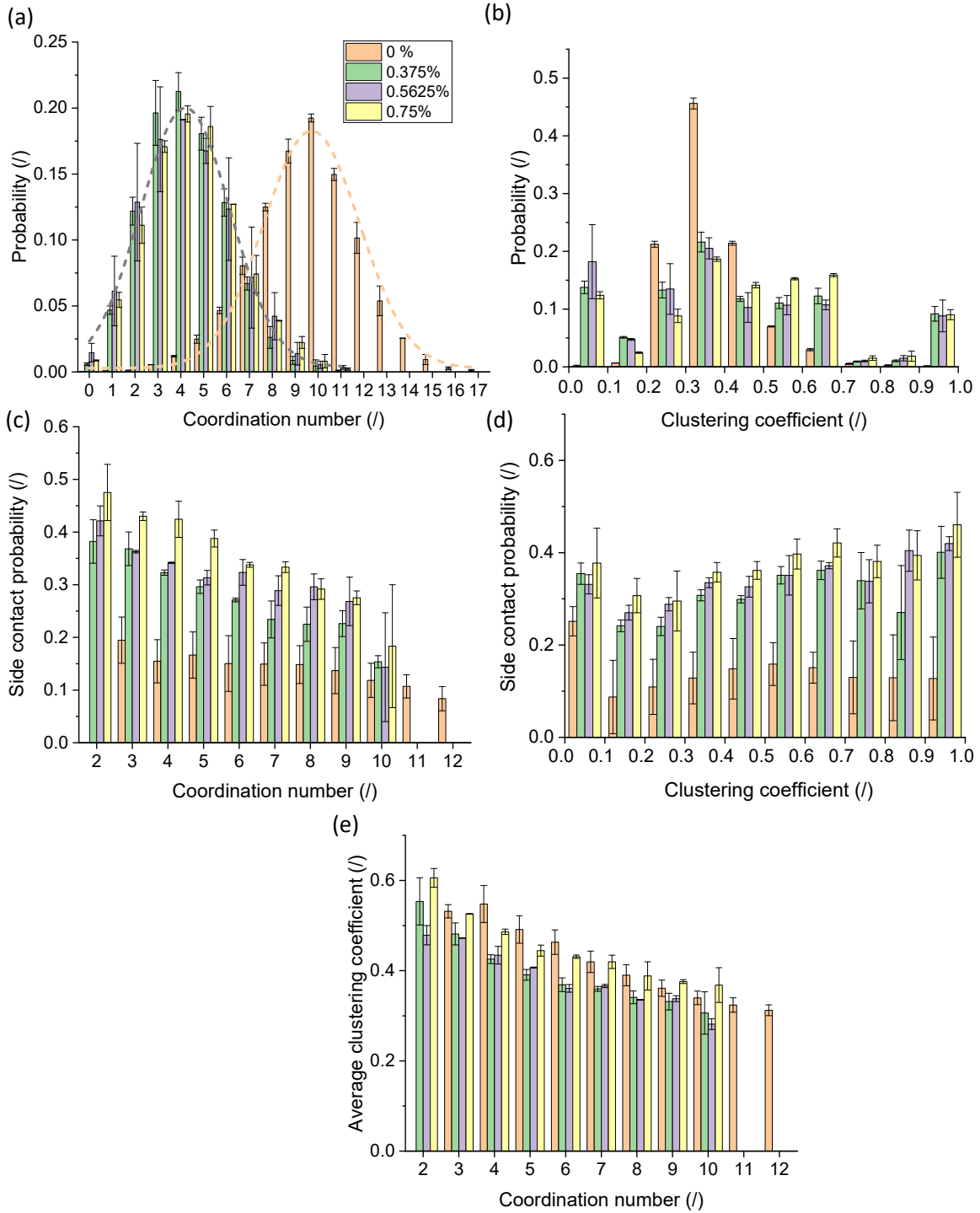


FIG. 5. Probability distribution of average (a) coordination number (z) and (b) clustering coefficient (c) with different amounts of secondary liquids. Average side contact probability distribution over (c) coordination number and (d) clustering coefficient with different amounts of secondary liquids. (e) Average clustering coefficient over coordination number. The gray and orange dashed lines in (a) show the fits for a normal distribution.

the more uniformly clustered structures seen in the suspension system.

The clustering coefficient distribution reveals notable characteristics at the extremes, specifically at $c = 0$ and $c = 1$, representing fully sparsely connected and clustered configurations, respectively. Mathematically, a low (but non-zero) c typically arises from structures with high z with few inter-neighbor clusters, while $c = 1$ does not restrict the number of neighboring particles. The peak at $c = 0$ can either arise via a sparse network of point-to-point contacts without trimers, or clusters of side-to-side contacts without any inter-connections (Supplementary Fig. S6). The average clustering coefficient decreases monotonically with coordination number across all secondary fluid volume fractions (Fig. 5e). While secondary fluid content shows limited impact on the averaged clustering behavior, the inverse relationship between clustering coefficient and coordination number suggests a fundamental transition in network topology: low coordination configurations ($z < 4$) display high clustering coefficients ($c \approx 0.5$), indicating locally dense arrangements, while higher coordination numbers ($z > 8$) correspond to more distributed structures with clustering coefficients $c < 0.4$.

As shown in the plot of side contact probability as a function of the clustering coefficient in Supplementary Fig. 5d, the percentage of side-to-side contacts generally increases with the clustering coefficient for the capillary suspensions, but there is a local maximum for $c < 0.1$. For the pure suspension, the side contact probability is significantly higher for $c < 0.1$, implying a flat structure without interconnects, likely caused by the sedimentation against the bottom plate, as shown on Fig. 3.

For particles with more neighboring particles (higher z), the network configuration becomes more difficult to fully cluster ($c = 1$) [32]. As can be seen from Supplementary Fig. S6, for a particle with $z = 6$, the theoretical maximum clustering coefficient for rods arranged in a hexagonal configuration with solely side-to-side contacts is limited to $c = 2/5$, and with pure point-to-point contacts, c can increase to $2/3$. To achieve a higher c in the range of $0.7 < c < 0.9$, it is required to have a $z > 4$, with specific configurations. Therefore, the probability is rather low. This suggests that highly clustered local structures are achieved through a combination of point-to-point and side-to-side contacts rather than maximizing lateral surface contacts between rods. The observed populations at $c = 1$ represent a special case, where the particles are mainly with a z of 2 or 3, with an even (50 : 50) contact type distribution (Fig. 5d). This implies that additional particle contacts tend to form with sparse, point-to-point neighbors rather than within side-to-side connected clusters. The result is a network where small bundles of side-to-side contacts are connected by

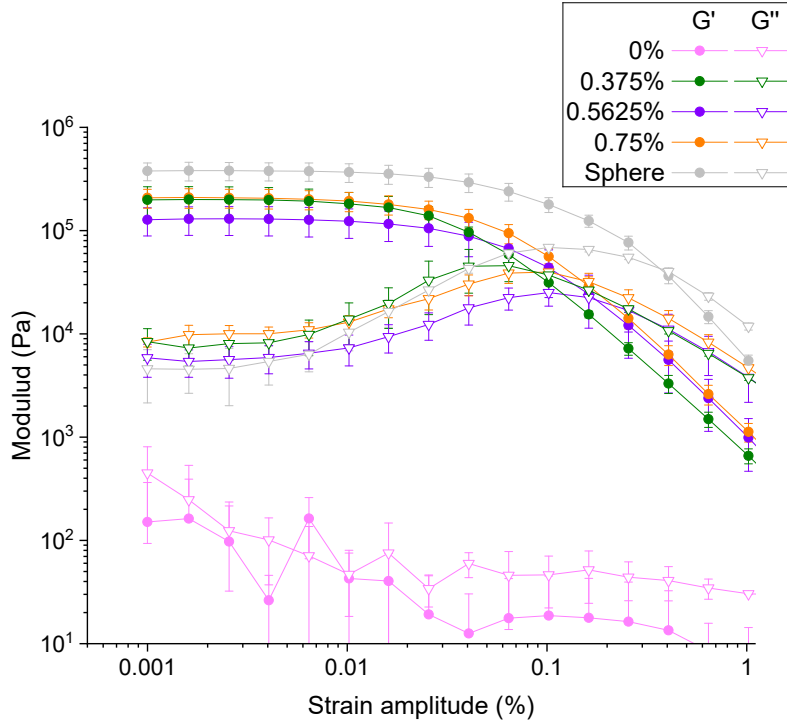


FIG. 6. Amplitude sweep of rod-based capillary suspensions with different amounts of secondary liquids. The data of the sphere microparticle based capillary suspension is taken from the previous research by Liu et al [30], with 20 vol% 10 μm microparticles and 1 vol% secondary liquid.

randomly oriented rods, with bundle size directly related to the secondary liquid fraction as shown in Fig. 5c.

B. Rheological measurements

Understanding the connection between microstructure and deformation is crucial for designing and optimizing capillary suspensions with anisotropic particles, as the orientation of the particles can greatly influence the rheological properties and functionality of the resulting materials. The moduli as a function of strain amplitude γ_0 (Fig. 6) reveals distinct rheological behaviors across different secondary fluid contents, particularly in comparison with pure suspension or capillary suspension using spherical particles. Rod-based systems with secondary fluid exhibit relatively short linear viscoelastic (LVE) regions, maintaining constant moduli only up to approximately 0.01% strain amplitude, beyond which both G' and G'' begin to deviate from linearity. In contrast,

the spherical particle system ($\phi_{solid} = 20\%$) shows an extended LVE region up to about 0.03% strain, suggesting a more robust network structure that can accommodate larger deformations without structural breakdown, possibly due to their isotropy and ability to rebuild bridges [30]. The suspension system shows negligible linear behavior, with nearly immeasurable moduli. In non-LVE region, for systems with $\phi_{sec} = 0.375\%$ (green), both moduli cross at the flow point ($G' = G''$), at $\gamma_0 < 0.1\%$. This short LVE region indicates the sensitivity of the rod-particle capillary network to deformation at low secondary liquid volume [13]. Systems with higher amounts of secondary fluid display the characteristic G'' overshoot near their flow points ($\gamma_0 \approx 0.16\%$ strain), followed by network breakdown. This behavior illustrates how particle geometry influences structural stability under deformation, with rod particles creating networks that are more sensitive to strain compared to their spherical counterparts. This explanation is supported using the viscoplasticity model proposed by Donley et al [33]. The real viscoplasticity value $N_{vpf}(\omega)$ can be expressed as [33],

$$N_{vpf}(\omega) = \max \left(\frac{\Delta G''_{fluid}(\omega)}{G''_{fluid}(\omega)} \right) \quad (5)$$

where the classical storage modulus G'' is divided into an elastic contribution G''_{solid} and a viscous contribution G''_{fluid} [33]. In the case of comparing samples of the same category with similar storage modulus G' behavior, the N_{vpf} can be simplified as $\max(\frac{\Delta G''}{\Delta \gamma})$, the maximum slope of modulus G'' divided by the strain for values after the LVE and before the G'' overshoot [33–35], i.e. $\gamma_0 = 0.006\text{--}0.04\%$. The corresponding fragility increases with the slope value, implying that the material more quickly acquires unrecoverable deformation. The G' slope of the four samples follows the order: sphere $> 0.375\text{ vol}\% > 0.5625\text{ vol}\% = 0.75\text{ vol}\%$ ($1.0 > 0.8 > 0.5 = 0.5 \times 10^6\text{ Pa}/\%$). This corresponds to the dominance of point-to-point contact in spherical systems, and the lower side-to-side contact probability in the 0.375 vol% sample. Point-to-point contacts enable a stiffer local structure where the stress starts to build up before the yielding occurs [35]. Capillary suspensions with more side-to-side contacts (clusters) distribute external forces over larger areas, resulting in a lower local modulus (rearrangement), showing a lower brittleness. For similar geometric systems, a higher brittleness denotes a lower critical strain [30, 35].

Rheological measurements alone do not fully elucidate the microstructural response of the system. Therefore, capillary suspension with 0.75 vol% secondary liquid was chosen to perform a rheoconfocal measurements due to its similar structure in comparison to the 0.5625 vol% sample but with an elevated average elastic modulus. An amplitude sweep was performed at the frequency

of 10 rad/s with an image plane at 36 μm of the total gap of 250 μm . The corresponding visual, rheological, and analyses are plotted in Fig. 7. Three timestamps (A, B, C) are chosen with positions corresponding to the shear strain amplitudes of $\gamma_0 = 0.26, 0.89$ and 3.72 %, the differences between the images at each strain are shown in Fig. 7a-c (where $\gamma_0 = 0.26$ % is compared to $\gamma_0 = 0$ %) in cyan with the local velocity vectors marked. The rheological measurement and mean displacement are plotted in Fig. 7d, with strains from Fig. 7a-c marked correspondingly. Before a strain amplitude of $\gamma_0 = 0.26$ %, marked as point A, the mean deformation in Fig. 7d is negligible, i.e. within the detection limits, and three clusters (ROI1-3) are observed with slight movements in different directions Fig. 7e, as plotted in the flow and vorticity directions. Due to the directionality of anisotropic particles, the displacement can also involve tumbling, which is retrieved from a 2d video of the particle using the mean ellipse aspect ratio (eAR) of the elliptically fitted particle cross-sections, as shown in Fig 7f. Since eAR values are inversely related to polar angles, particles with an eAR of unity indicate $\varphi = 90^\circ$, with φ decreasing with increasing eAR. As shown in Fig 7f, the average eAR for each ROI differs from each other, but the eAR for each particle in the cluster is highly uniform (light points), as expected for side-to-side contacts.

The end of the LVE region ($\gamma_0 = 0.26\text{--}0.89$ %, between points a and b) marks the onset of particle rearrangement. This region typically indicates that the elastic deformation becomes unsustainable and the network starts to rupture allowing relative movement between particles [36]. This is visually proven by the enhanced mean displacement (Fig. 7d), movement of clusters in ROI1 and 3 in flow and vorticity directions respectively (Fig. 7e), and the drop in their average eAR (Fig. 7f), indicating particle tumbling in addition to displacement (Fig. 7e). Interestingly, the three particle clusters all move in different directions – ROI1 moves in the flow direction and rotates from a higher eAR to lower (decreasing φ), ROI2 remains in the same position and exhibits only a slight increase in the eAR, and ROI3 displaces in the negative vorticity direction with the eAR decreasing on average with high variability.

At a strain amplitude of $\gamma_0 = 0.89$ % (point B), the mean displacement reaches a maximum, likely denoting the limit of elastic deformation where particles are stretched to their maximum reversible configuration before bonds begin to break. Shortly after, the flow point, where the network starts to fluidize with majorly irreversible plastic flow [37], is reached and the network breaks into shear and unsheared parts [38]. During this process, the bonds where the exerted forces are translated from top plate break, resulting in decreased mean displacement [6]. This flow point in Fig. 7d ($\gamma_0 = 1$ %), is prolonged in comparison to that shown in Fig. 6, potentially due

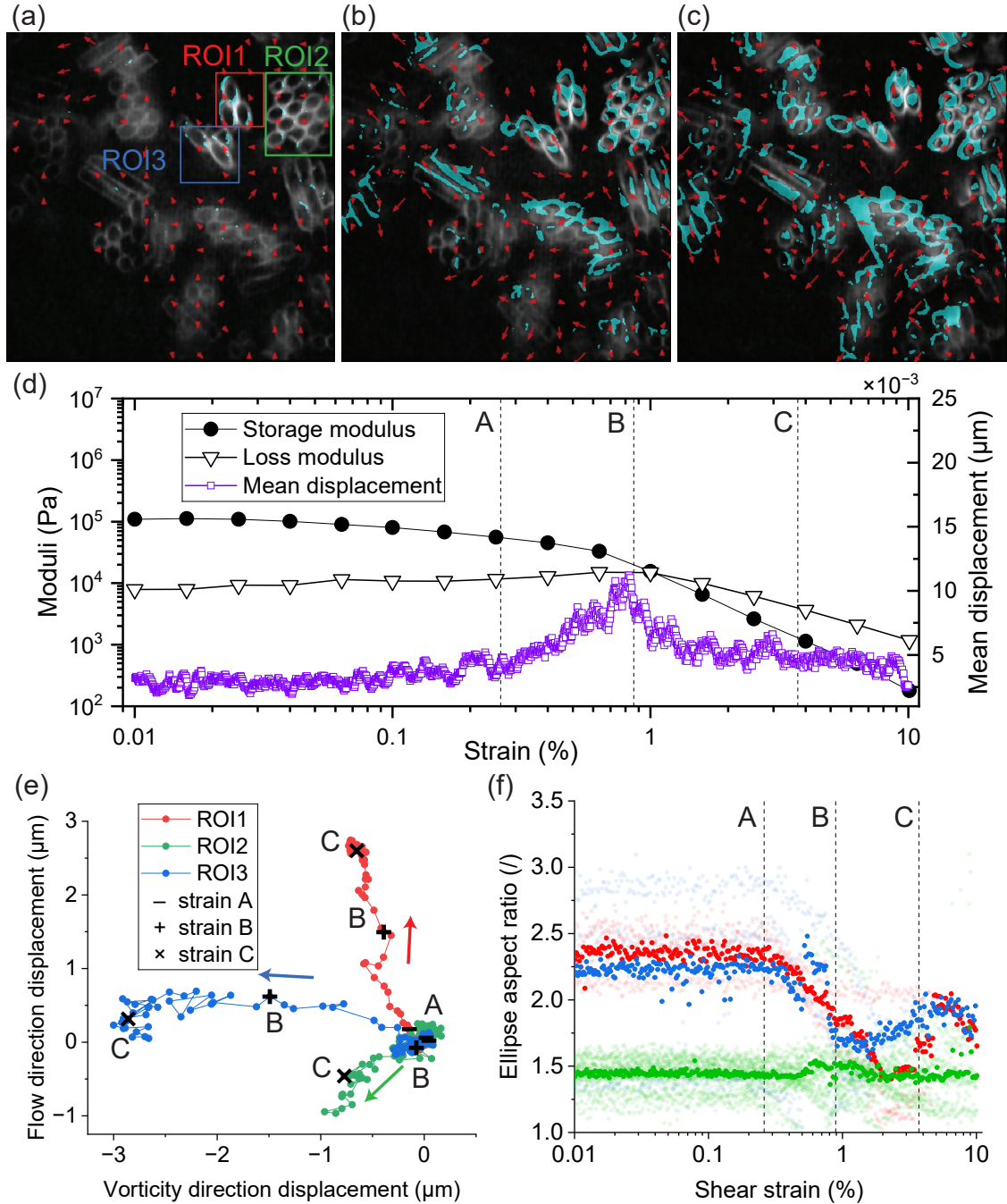


FIG. 7. An amplitude sweep was performed on the rheoconfocal microscopy with an gap of $250 \mu\text{m}$, the image plane was at $36 \mu\text{m}$. Three images were chosen with positions corresponding to the shear strain amplitudes of $\gamma_0 = 0.26, 0.89$ and 3.72% . (a-c) Each image is superimposed on the previous one, the differences are shown in cyan pixels and the displacement vectors $\Delta\vec{r}$ are represented by the red arrows, indicating the local displacement within a box of 80 pixel ($21.6 \mu\text{m}$) square. (d) the shear moduli and the mean displacement are plotted over the strain. The displacement in both flow and vorticity direction, and averaged circularity of each particle of the clusters in ROI1,2, and 3 are as shown in (e) and (f) respectively.

to a combined effect of enhanced wall slip due to smooth bottom plate (glass for observation) [6, 38, 39] and the increase in side-to-side contact clusters [33, 35] due to compression caused by rheoconfocal thin film loading technique. Post-yielding, e.g. point C, the apparent strain recorded by the rheometer differs from the real strain in the sample due to the slip layer near the top and bottom plates [40]. During this stage, the average displacement of the sample gradually returns to zero. The network structure is disrupted and capillary bridges break, as indicated by cyan in Fig. 7c. The density of particles in this shear plane near the bottom of the plate increase with some of particles perpendicular to the shear gradient (cyan marked rectangular particles with high φ). Accordingly, the eAR values of the clusters fluctuate from shortly prior to point B to after point C, consistent with particle rotation. These three clusters each move randomly, without a clear correlation to the flow direction with the cluster in ROI2 remaining relatively stationary.

IV. CONCLUSION

The study of rod-based capillary suspensions reveals the intriguing interplay between secondary liquid content, particle interactions, and the corresponding microstructure. The present paper demonstrates that capillary forces have a profound influence on particle orientation and network formation, greatly decreasing the onset volume fraction of inducing yield stresses. As the secondary liquid volume increases, the contact type transforms from point-to-point contact to side-to-side contacts. Meanwhile, the coordination number and clustering are inversely correlated. Unlike spherical particle systems [13, 20], the rod-based capillary suspensions exhibit a complex clustering behavior where increased coordination does not simply lead to more uniform, smectic liquid crystal-type local arrangement.

By categorizing the rod particle contact type, we offer a novel methodology to design the microstructure of capillary suspension by changing the secondary liquid volume fractions, and the corresponding rheological response can be predicted. Our rheological measurements denote the unique mechanical sensitivity of these anisotropic networks. The shorter linear viscoelastic regions and distinctive deformation responses highlight the critical role of particle contact configuration in determining material properties. Rheoconfocal measurement further uncovers the chaotic nature of cluster movement, revealing the nuanced local mechanical responses that are different from our macroscopic observations.

Our research paves the way of using rod-based capillary suspensions as a versatile precursor for

advanced material design. By precisely controlling secondary liquid content and particle interactions, we can create materials with unknown structural complexity and tailored functionality. The correlation between particle orientation, network formation, and their mechanical responses opens new doors for developing smart, adaptable materials with applications ranging from 3D printing ceramics to novel food fabrications.

AUTHOR CONTRIBUTIONS

Lingyue Liu: Conceptualization, Methodology, Software, Investigation, Writing – original draft. **Sebastian Gassenmeier:** Methodology, Software. **Erin Koos:** Funding acquisition, Conceptualization, Methodology, Writing – review & editing, Supervision.

ACKNOWLEDGEMENTS

The authors would like to thank financial support from the European Union’s Horizon 2020 research and innovation programme under the Marie Skłodowska-Curie grant agreement No 955612 and International Fine Particle Research Institute (IFPRI).

-
- [1] S. J. Ahn, K. H. Ahn, and S. J. Lee, Film squeezing process for generating oblate spheroidal particles with high yield and uniform sizes, [Colloid and Polymer Science](#) **294**, 859 (2016).
 - [2] J. Férec, G. Ausias, M. C. Heuzey, and P. J. Carreau, Modeling fiber interactions in semiconcentrated fiber suspensions, [Journal of Rheology](#) **53**, 49 (2009).
 - [3] M. J. Solomon and P. T. Spicer, Microstructural regimes of colloidal rod suspensions, gels, and glasses, [Soft Matter](#) **6**, 1391 (2010), publisher: The Royal Society of Chemistry.
 - [4] E. P. Lewandowski, J. A. Bernate, A. Tseng, P. C. Searson, and K. J. Stebe, Oriented assembly of anisotropic particles by capillary interactions, [Soft Matter](#) **5**, 886 (2009), publisher: The Royal Society of Chemistry.
 - [5] K. J. Lee, J. Yoon, and J. Lahann, Recent advances with anisotropic particles, [Current Opinion in Colloid & Interface Science](#) **16**, 195 (2011).
 - [6] S. Mueller, E. W. Llewellyn, and H. M. Mader, The rheology of suspensions of solid particles, [Proceedings of the Royal Society A: Mathematical, Physical and Engineering Sciences](#) **466**, 1201 (2009).

- [7] M. Khan, R. V. More, L. Brandt, and A. M. Ardekani, Rheology of dense fiber suspensions: Origin of yield stress, shear thinning, and normal stress differences, [Physical Review Fluids](#) **8**, 064306 (2023).
- [8] O. Ranquet, C. Duce, E. Bramanti, P. Dietemann, I. Bonaduce, and N. Willenbacher, A holistic view on the role of egg yolk in Old Masters' oil paints, [Nature Communications](#) **14**, 1534 (2023).
- [9] D. Menne, L. Lemos da Silva, M. Rotan, J. Glaum, M. Hinterstein, and N. Willenbacher, Giant Functional Properties in Porous Electroceramics through Additive Manufacturing of Capillary Suspensions, [ACS Applied Materials & Interfaces](#) **14**, 3027 (2022).
- [10] M. Weiß, P. Sälzler, N. Willenbacher, and E. Koos, 3D-Printed lightweight ceramics using capillary suspensions with incorporated nanoparticles, [Journal of the European Ceramic Society](#) **40**, 3140 (2020).
- [11] L. Liu, M. Abbot, P. Brockmann, I. V. Roisman, J. Hussong, and E. Koos, Dewetting Fingering Instability in Capillary Suspensions: Role of Particles and Liquid Bridges, [Langmuir](#) **41**, 5399 (2025).
- [12] E. Koos and N. Willenbacher, Capillary Forces in Suspension Rheology, [Science](#) **331**, 897 (2011), publisher: American Association for the Advancement of Science.
- [13] J. Allard, S. Burgers, M. C. Rodríguez González, Y. Zhu, S. De Feyter, and E. Koos, Effects of particle roughness on the rheology and structure of capillary suspensions, [Colloids and Surfaces A: Physicochemical and Engineering Aspects](#) **648**, 129224 (2022).
- [14] F. Bossler, L. Weyrauch, R. Schmidt, and E. Koos, Influence of mixing conditions on the rheological properties and structure of capillary suspensions, [Colloids and Surfaces A: Physicochemical and Engineering Aspects](#) **518**, 85 (2017).
- [15] F. Bossler, J. Maurath, K. Dyhr, N. Willenbacher, and E. Koos, Fractal approaches to characterize the structure of capillary suspensions using rheology and confocal microscopy, [Journal of Rheology](#) **62**, 183 (2018).
- [16] I. Natalia, R. H. Ewoldt, and E. Koos, Particle contact dynamics as the origin for noninteger power expansion rheology in attractive suspension networks, [Journal of Rheology](#) **66**, 17 (2022), publisher: The Society of Rheology.
- [17] R. Kazama, Y. Murakami, and A. Shono, Microstructure and rheological behavior of capillary suspension prepared with plate-shaped particles, [Colloids and Surfaces A: Physicochemical and Engineering Aspects](#) **637**, 128254 (2022).
- [18] J. Maurath, B. Bitsch, Y. Schwegler, and N. Willenbacher, Influence of particle shape on the rheological behavior of three-phase non-brownian suspensions, [Colloids and Surfaces A: Physicochemical and](#)

- [Engineering Aspects](#) **497**, 316 (2016).
- [19] Y. Qiao, S. Xiang, Y. Huang, C. Mao, M. Kong, Q. Yang, and G. Li, Microstructure of Rod-Based Capillary Suspensions with Different Rod Aspect Ratios under Quiescent and Shear Flow, [Industrial & Engineering Chemistry Research](#) **58**, 9422 (2019).
- [20] S. Bindgen, F. Bossler, J. Allard, and E. Koos, Connecting particle clustering and rheology in attractive particle networks, [Soft Matter](#) **16**, 8380 (2020).
- [21] S. Bindgen, J. Allard, and E. Koos, The behavior of capillary suspensions at diverse length scales: from single capillary bridges to bulk, [Current Opinion in Colloid & Interface Science](#) **58**, 101557 (2022), arXiv:2107.14714 [cond-mat].
- [22] E. R. Weeks, J. C. Crocker, A. C. Levitt, A. Schofield, and D. A. Weitz, Three-Dimensional Direct Imaging of Structural Relaxation Near the Colloidal Glass Transition, [Science](#) **287**, 627 (2000), publisher: American Association for the Advancement of Science.
- [23] S. Li, J. Zhao, P. Lu, and Y. Xie, Maximum packing densities of basic 3D objects, [Chinese Science Bulletin](#) **55**, 114 (2010).
- [24] D. C. C. Lam, Packing model for bimodal particle packing with aligned fibers, [Journal of Materials Processing Technology](#) **79**, 170 (1998).
- [25] H. M. Princen, Capillary phenomena in assemblies of parallel cylinders: I. Capillary rise between two cylinders, [Journal of Colloid and Interface Science](#) **30**, 69 (1969).
- [26] H. M. Princen, Capillary phenomena in assemblies of parallel cylinders: II. Capillary rise in systems with more than two cylinders, [Journal of Colloid and Interface Science](#) **30**, 359 (1969).
- [27] H. M. Princen, Capillary phenomena in assemblies of parallel cylinders: III. Liquid Columns between Horizontal Parallel Cylinders, [Journal of Colloid and Interface Science](#) **34**, 171 (1970).
- [28] Y. I. Rabinovich, M. S. Esayanur, and B. M. Moudgil, Capillary forces between two spheres with a fixed volume liquid bridge: theory and experiment, [Langmuir: the ACS journal of surfaces and colloids](#) **21**, 10992 (2005).
- [29] M. Scheel, R. Seemann, M. Brinkmann, M. Di Michiel, A. Sheppard, B. Breidenbach, and S. Herminghaus, Morphological clues to wet granular pile stability, [Nature Materials](#) **7**, 189 (2008), number: 3 Publisher: Nature Publishing Group.
- [30] L. Liu, J. Allard, and E. Koos, Enhanced contact flexibility from nanoparticles in capillary suspensions, [Journal of Colloid and Interface Science](#) **665**, 643 (2024).

- [31] A. Wouterse, S. Luding, and A. P. Philipse, On contact numbers in random rod packings, [Granular Matter](#) **11**, 169 (2009).
- [32] S. Torquato and F. H. Stillinger, Jammed hard-particle packings: From Kepler to Bernal and beyond, [Reviews of Modern Physics](#) **82**, 2633 (2010).
- [33] G. J. Donley, J. R. de Bruyn, G. H. McKinley, and S. A. Rogers, Time-resolved dynamics of the yielding transition in soft materials, [Journal of Non-Newtonian Fluid Mechanics](#) **264**, 117 (2019).
- [34] K. Kamani, G. J. Donley, and S. A. Rogers, Unification of the Rheological Physics of Yield Stress Fluids, [Physical Review Letters](#) **126**, 218002 (2021), publisher: American Physical Society.
- [35] K. M. Kamani and S. A. Rogers, Brittle and ductile yielding in soft materials, [Proceedings of the National Academy of Sciences](#) **121**, e2401409121 (2024).
- [36] A. Z. Nelson, K. S. Schweizer, B. M. Rauzan, R. G. Nuzzo, J. Vermant, and R. H. Ewoldt, Designing and transforming yield-stress fluids, [Current Opinion in Solid State and Materials Science](#) **23**, 100758 (2019).
- [37] D. Bonn, M. M. Denn, L. Berthier, T. Divoux, and S. Manneville, Yield stress materials in soft condensed matter, [Reviews of Modern Physics](#) **89**, 035005 (2017).
- [38] A. Yamamoto, T. Inui, D. Suzuki, and K. Urayama, Stress-independent delay time in yielding of dilute colloidal gels, [Soft Matter](#) **19**, 9082 (2023).
- [39] H. J. Walls, S. B. Caines, A. M. Sanchez, and S. A. Khan, Yield stress and wall slip phenomena in colloidal silica gels, [Journal of Rheology](#) **47**, 847 (2003).
- [40] V. Bertola, F. Bertrand, H. Tabuteau, D. Bonn, and P. Coussot, Wall slip and yielding in pasty materials, [Journal of Rheology](#) **47**, 1211 (2003).

SUPPLEMENTARY MATERIAL

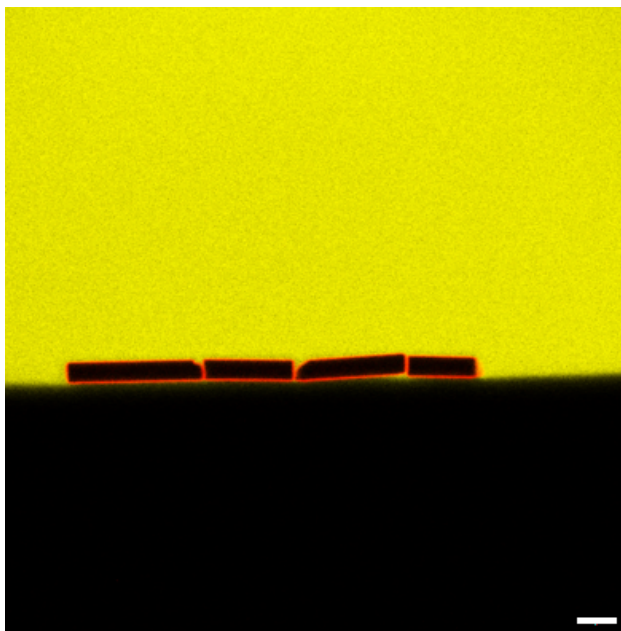


FIG. S1. Contact angle measurement of rod particles at bulk (black) and secondary liquid (yellow) interfaces. The scale bar is $10\ \mu\text{m}$.

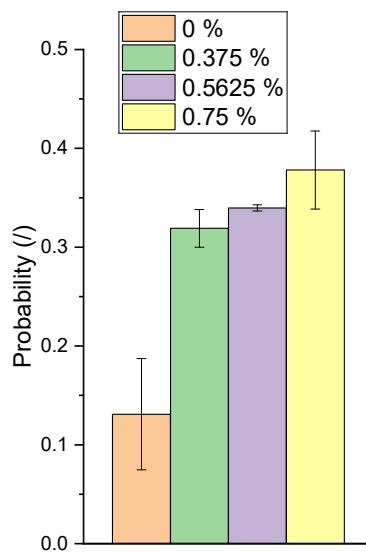


FIG. S2. Averaged side contact probability with different amounts of secondary liquids

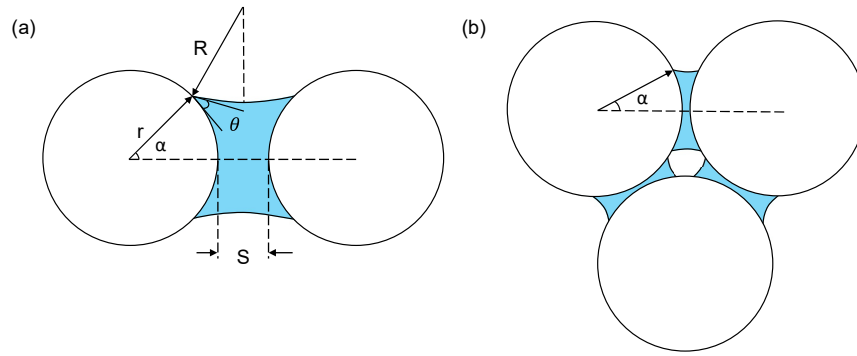


FIG. S3. Cross section of a liquid bridge between (a) two (b) three parallel rods in the central region.

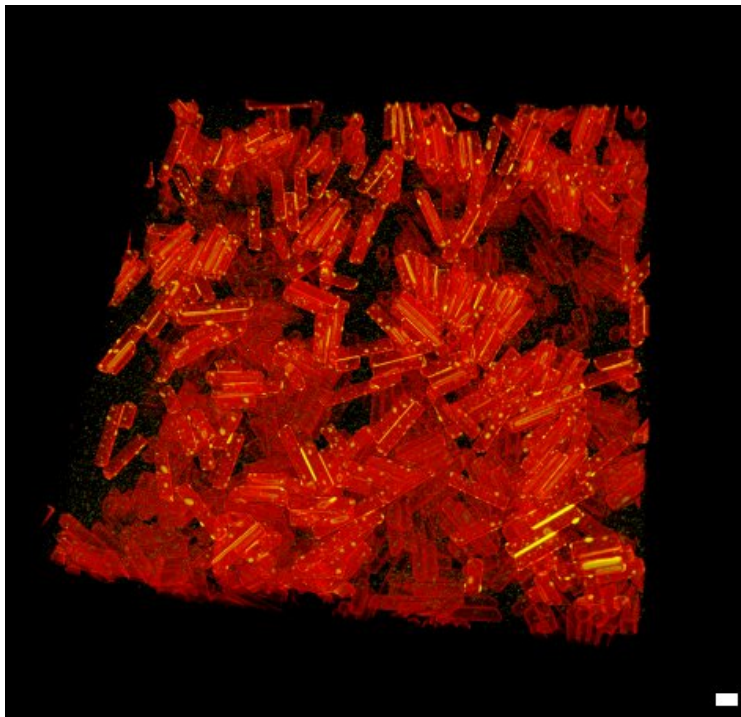


FIG. S4. 3D reconstructed confocal micrographs of capillary suspension with a secondary liquid of 0.75 % ($\phi_{\text{sec}}/\phi_{\text{solid}} = 5\%$), the scale bar is 10 μm .

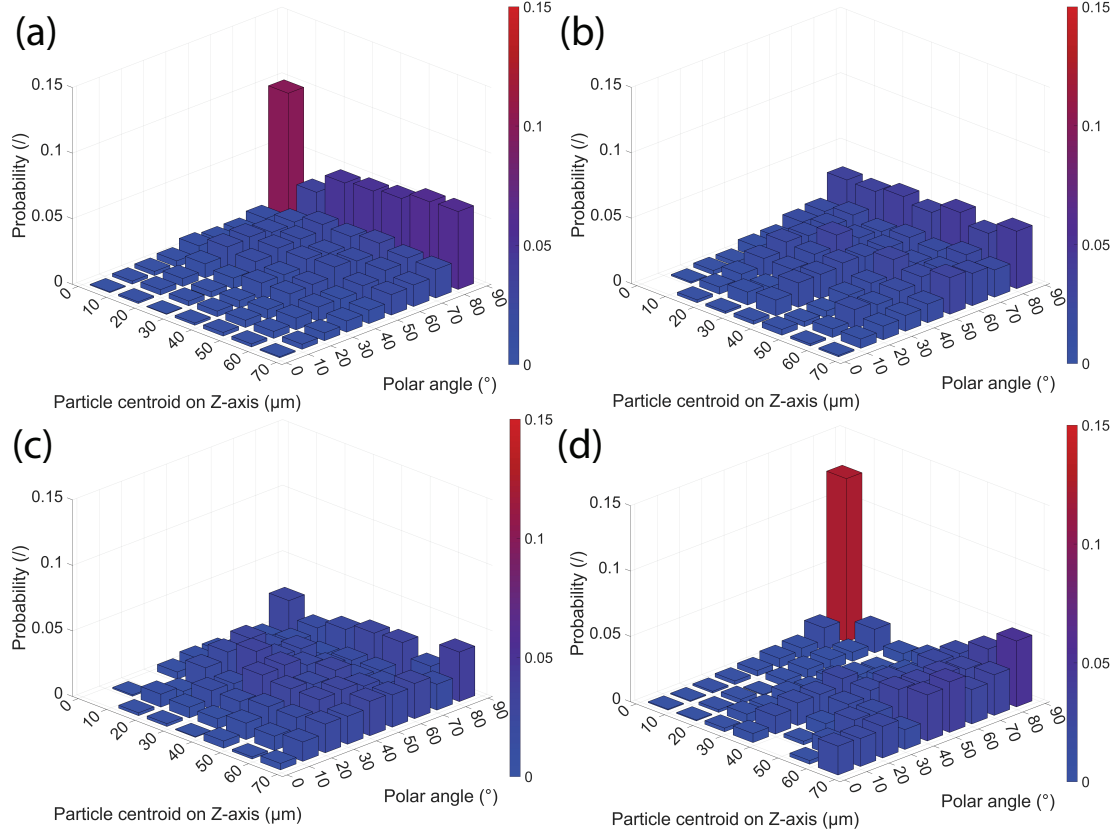


FIG. S5. Polar angle probability as a function of particle position in capillary suspensions with different amounts of secondary liquid (a) 0 % ($\phi_{\text{sec}}/\phi_{\text{solid}} = 0.0$ %) (b) 0.375 % ($\phi_{\text{sec}}/\phi_{\text{solid}} = 2.5$ %) (c) 0.5625 % ($\phi_{\text{sec}}/\phi_{\text{solid}} = 3.75$ %) (d) 0.75 % ($\phi_{\text{sec}}/\phi_{\text{solid}} = 5$ %).

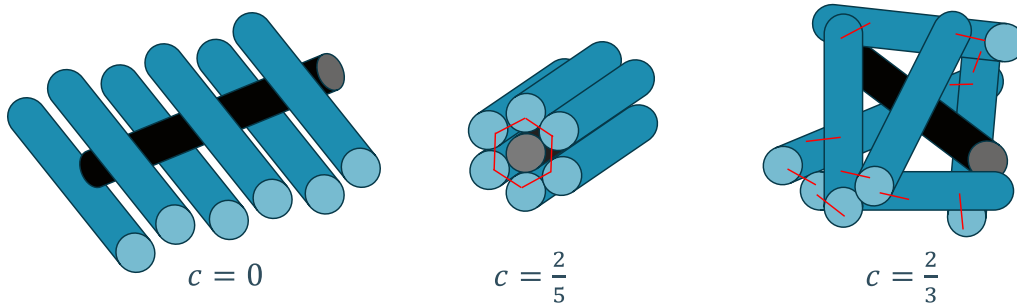


FIG. S6. Schematic showing the clustering coefficient for various configurations of rods with a coordination number of 6 in 3D.